The merging of Kelvin–Helmholtz vortices into large coherent flow structures in a high Reynolds number flow past a wall-mounted square cylinder

Philippe Mercier, Maria Ikhennicheu, Sylvain Guillou, Grégory Germain, Emmanuel Poizot, Mikaël Grondeau, Jérôme Thiebot, Philippe Druault

Ocean Engineering
May 2020, Volume 204 Pages 107274 (13p.)
https://doi.org/10.1016/j.oceaneng.2020.107274
https://archimer.ifremer.fr/doc/00617/72940/

The merging of Kelvin–Helmholtz vortices into large coherent flow structures in a high Reynolds number flow past a wall-mounted square cylinder

Mercier Philippe [1, *] , Ikhennicheu Maria [2], Guillou Sylvain [1], Germain Gregory [2], Poizot Emmanuel [1], Grondeau Mikaël [1], Thiébot Jérôme [1], Druault Philippe [3]

[1] Normandie Université, UNICAEN LUSAC, EA 4253, 60 rue Max Pol Fouchet, CS 20082, 50130 Cherbourg-en-Cotentin, France
[2] Ifremer, Marine Structure Laboratory, 150 Quai Gambetta 62200 Boulogne sur Mer, France
[3] Sorbonne Université, CNRS, UMR 7190, Institut Jean Le Rond d'Alembert, F-75005 Paris, France

* Corresponding author : Philippe Mercier, email address : philippe.mercier@unicaen.fr

Abstract :

Flows at tidal-stream energy sites are characterised by high turbulence intensities and by the occurrence of highly energetic large and coherent flow structures. The interaction of the flow with seabed roughness is suspected to play a major role in the generation of such coherent flow structures. The problem is introduced with canonical wall-mounted square obstacles representing abrupt changes of bathymetry, with high Reynolds number flow (Re = 250000). Two methods are used: a numerical model, based on the LBM (Lattice Boltzmann Method) combined with LES (Large Eddy Simulation) and an experimental set-up in a circulating tank. The numerical model is validated by comparison with experimental data. In the case of a wall-mounted square cylinder, large-scale turbulent structures are identified in experiments where boils at the free surface can be observed. LBM simulation allows their three-dimensional characterisation. The dynamic of such large-scale events is investigated by temporal, spatial and spectral numerical analysis. Results show that periodical Kelvin–Helmholtz vortices are emitted in the cylinder wake. Then, they merge to form larger and more coherent structures that rise up to the surface. A wavelet study shows that the emission frequency of the Kelvin–Helmholtz vortices is not constant over time.

Highlights

► The lattice Boltzmann method properly simulate rough flows using a coarse mesh. ► Kelvin–Helmholtz vortices are released in a wall-mounted square cylinder wake. ► Kelvin–Helmholtz vortices merge into large boils ► The Kelvin–Helmholtz vortex emission frequency is not stable in time.

Keywords : Turbulence, Coherent flow structure, Numerical simulation, Lattice Boltzmann, Method, Large Eddy Simulation, Wall-mounted obstacles

1. Introduction

Tidal energy harvesting is a booming industry and new industrial projects are emerging. French waters are one of the largest tidal potential: they represent 25% of the European potential [EDF (2010)]. High turbulence intensities are measured in the water column at tidal sites, typically around 10 to 20% [Thomson et al. (2012)], [McMillan et al. (2017)]. Velocity fluctuations can have a significant impact both on the production of tidal turbines [Duràn Medina et al. (2017)] and on their structural fatigue [Mycek et al. (2014)]. It is therefore essential to characterise turbulence at tidal-stream energy sites. Some very energetic turbulent events can rise up to the surface [Best (2005)]. The physical phenomena involved in the generation and the evolution of such coherent flow structures are not yet understood. Figure 1 illustrates bathymetry variations over a $\sim 400 \times 1000\ m^2$ area of interest for tidal turbine application in the Alderney Race, with currents reaching 5 $m.s^{-1}$. A high diversity of bathymetric reliefs is observed including plateaus, abrupt breaks or huge elevations, which may play a role in the generation of highly turbulent flows and large coherent flow structures. In order to investigate the turbulence generation process in this specific area and due to the complexity of *in situ* study, a first approach at a laboratory scale

*Corresponding author
Email address: philippe.mercier@unicaen.fr (Philippe Mercier)

is necessary.

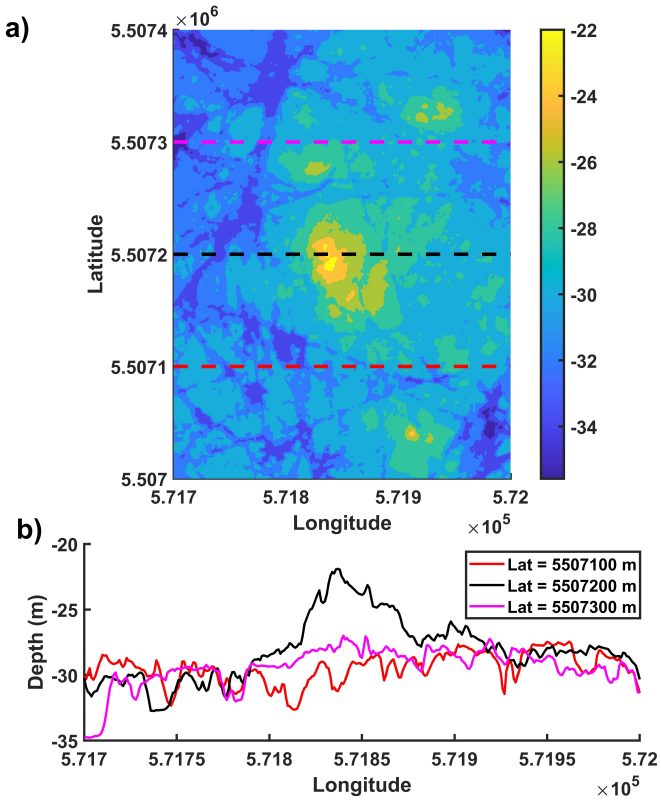

Figure 1: Bathymetry of the Alderney Race area. Data from [SHOM (2015)]. Coordinates from UTM 30 North. Depth are indicated relative to the hydrographic zero.

The literature provides many experimental and numerical studies of turbulent flows above uneven walls. Such studies were conducted on realistic environmental geometries as dune or pebble beds or on idealised geometries such as flat planes, flat planes with individual obstacles or canopies. They highlighted physical phenomena involved in the generation of coherent flow structures. [Matthes (1947)] proposed a classification of turbulent events occurring in environmental flows and in particular described coherent turbulent motions generated at the flow bed and reaching the water surface. The pairing of Kelvin-Helmholtz vortex to form larger coherent flow structures was described by [Chandrsuda et al. (1978)] based on their experimental work on a flat plate and by [Müller, Gyr (1986)] on experimental two-dimensional dunes. Numerical simulation by [Comte et al. (1998)] allows studying this pairing through quantities that are difficult to access in experiments such as pressure. [Kwoll et al. (2017)] showed that pairing may occur within the shear layer and also through re-circulation of vortices downstream dunes.

Studies of canonical individual geometries highlight the influence of the shape and dimensions of a macro-roughness on the wake turbulence characteristics and on the production of coherent flow structures. General characteristics of the flow downstream of a macro-roughness are described by [Castro, Robins (1977)] on a cubic obstacle and by [Panigrahi, Acharya (2004)] on a rib. The generation of Kelvin-Helmholtz vortices on a wide geometry is visualised with high precision on numerical simulations by [Diabil et al. (2017)] or by [Cimarelli et al. (2018)] for a low Reynolds number flow. As for dune cases, such vortices may merge into large coherent flow structures in the case of a wall-mounted cylinder [Testik et al. (2005)], [Tang et al. (2017)]. Some coherent flow structures reach the flow surface in experiments [Zhong et al. (2015)], as observed in real tidal flow contexts.

Such idealised obstacles are however far from realistic seabed. Studies of canopy flows use multiple obstacles to model the effect of environmental flow bed roughness. Numerical studies conducted by [Coceal et al. (2007)] or [Anderson et al. (2015)] and experimental study conducted by [Florens et al. (2013)] showed generation of similar coherent flow structures on flow above square macro-roughness beds. Even more realistic study describes coherent flow structure generation above a pebble bed [Hardy et al. (2016)]. However, studies are often limited to moderate Reynolds numbers, or to geometries that are not representative of the seabed morphology of the Alderney Race.

In the perspective of the unsteady simulation of tidal flow above real seabed morphology, the choice of a numerical method adapted to this large and complex target case is crucial to limit computational resource needs. The Lattice Boltzmann Method (LBM) is derived from the gas kinetic theory [Bhatnagar et al. (1954)]. It numerically solves the Boltzmann equation on the nodes of a Cartesian grid, and is used to simulate flows [Qian et al. (1992)]. Its execution is simple, thus it is well suited for massively parallel use on heavy meshes of complex geometries [Succi et al. (1989)].

In the present contribution, LBM is combined with Large Eddy Simulation (LES). LES first appeared in the work of [Smagorinsky (1963)]. The purpose of LES is to reduce computational needs. The effect of small turbulence scales is modelled by a sub-grid model, which allows reducing the mesh resolution. A complete description of the method is found in [Sagaut (2006)]. LBM-LES numerical simulation specificities make it adequate for simulation of unsteady environmental flows. It has been punctually used for environmental simulations [Parmigiani (2013)] and flow around a wind turbine [Xu (2016)]. It is thus chosen here to investigate the physical process of coherent flow structure generation over roughnesses representative of real environmental obstacles.

In order to investigate the turbulence triggered by the seabed morphology, wall-mounted cubic obstacles are studied both experimentally in a circulating tank and numerically with the LBM-LES method at a 1/20 scale in a high Reynolds number flow ($R_e = 2.5 \times 10^5$). These ideal and controlled environments are suited to study how coherent flow structures form, interact and evolve in the turbulent wake of bathymetric variations. At first, the experimental set-up and the numerical model are presented. Model validation is achieved with wall-mounted cube and cylinder cases. Then, the wake development and vortices emitted past a wall-mounted cylinder are investigated through numerical simulation.

2. Methods

For this study, experimental and numerical tools are complementary. The experiment provides reliable data with determined error margins, but with limited access to information due to 2-components measurement techniques. Numerical simulation provides three-dimensional vision of the flow, the tracking of turbulent events through the whole domain and easy access to physical quantities such as pressure. However, the adequacy of the simulation with real flow has to be assessed. In this section, the experimental set-up is presented as well as the numerical methodology. Then a first case study of a wall-mounted cube is conducted with both methods to validate numerical simulation parameters.

2.1. Experimental set-up

Tests are carried out in the wave and current circulating flume tank of IFREMER located in Boulogne-sur-Mer (France) presented in Figure 2a. The incoming flow is assumed steady and constant. The test section is 18 m long $\times$ 4 m wide $\times$ 2 m deep. The three instantaneous velocity components are denoted as (U, V, W) along the (X, Y, Z) directions respectively (Figure 2b). Using the Reynolds decomposition, each instantaneous velocity component is separated into a mean value and a fluctuation component: $U = \overline{U} + u'$, where an overbar indicates the time average. H is the height of the studied obstacle. By

means of a grid combined with a honeycomb (that acts as a flow straightener) placed at the inlet of the working section (see Figure 2b), a low turbulent intensity of $I = 1.5$ % is achieved. Turbulence intensity I in the incoming flow is defined by Equation 1. The ∞ subscript stands for velocity in the far upstream that is not disturbed by the experimental object.

$$I = 100\sqrt{\frac{\frac{1}{3}(\overline{u'^2} + \overline{v'^2} + \overline{w'^2})}{\overline{U_\infty}^2 + \overline{V_\infty}^2 + \overline{W_\infty}^2}} \tag{1}$$

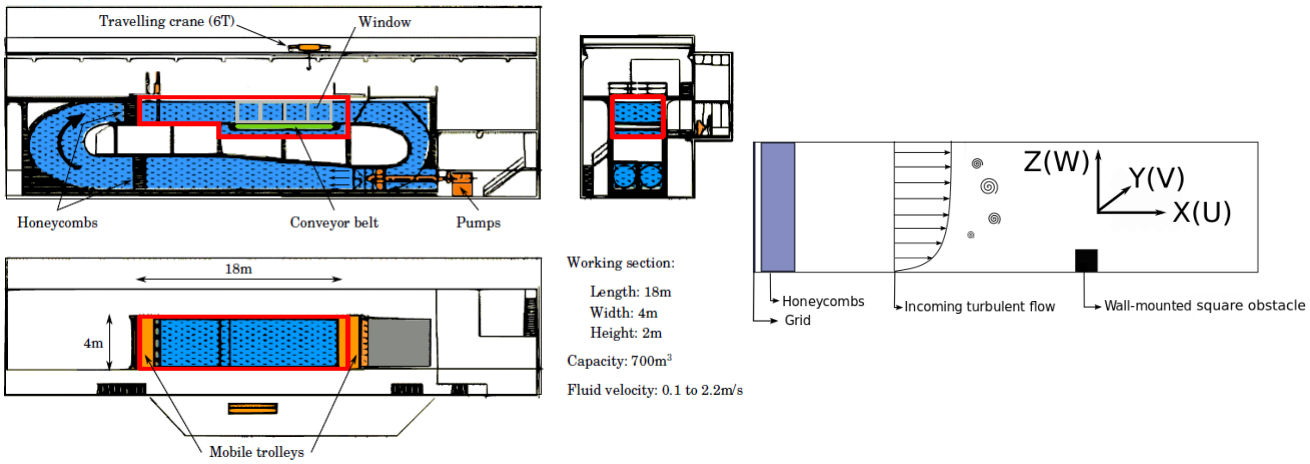

(a) IFREMER flume tank in Boulogne-sur-Mer. (b) Schematic view of an obstacle in the tank.

Figure 2: Representation of the IFREMER wave and current circulating tank in Boulogne-sur-Mer (France).

	Scale	U_∞ $[m.s^{-1}]$	Rugosity height H [m]	Depth D [m]	$R_e = \frac{HU_\infty}{\nu}$	$F_r = \frac{U_\infty}{\sqrt{gD}}$
Alderney Race	1	5	5	40	2.5×10^7	0.25
Flume tank	$\frac{1}{20}$	1	0.25	2	2.5×10^5	0.23

Table 1: *In situ* and experimental conditions.

Non dimensional quantities are based on the obstacle height H and the inflow fluid velocity U_∞. These quantities are indexed by *: $x^* = x/H$ and $t^* = tU_\infty/H$ for instance. In order to consider the interaction of turbulent events with the free surface, experiments are carried out with respect to Froude similitude (see Table 1) where $F_r = \frac{U_\infty}{\sqrt{gD}}$ with g the gravity and D the water depth. Furthermore, Reynolds number must be as high as achievable to be closer to real conditions. Two wall-mounted elements are studied: a cube and a square cylinder with a 6 aspect ratio in the lateral dimension. Their height is $H = 0.25\ m$, which is representative of 5-metre high obstacles in the Alderney Race.

Two Laser Velocimetry techniques are used: LDV (Laser Doppler Velocimetry) and PIV (Particle Image Velocimetry), see Figure 4. Beforehand, the tank is seeded with 10 μm diameter silver coated glass particles. For the PIV measurements, a Nd-YAG Laser GEMINI-LIKE is used: power is 200 mJ per probe and wavelength is 532 mm. It is synchronised with a Camera FLOWSENS EO-2M 1600 $pixels \times 1200\ pixels$ which acquires double images with a time step of 800 μs for the cube case and 1600 μs for the cylinder case. A particle is detected on 3 to 5 pixels, cross-correlation peak intensity is between 0.3 and 0.8 and

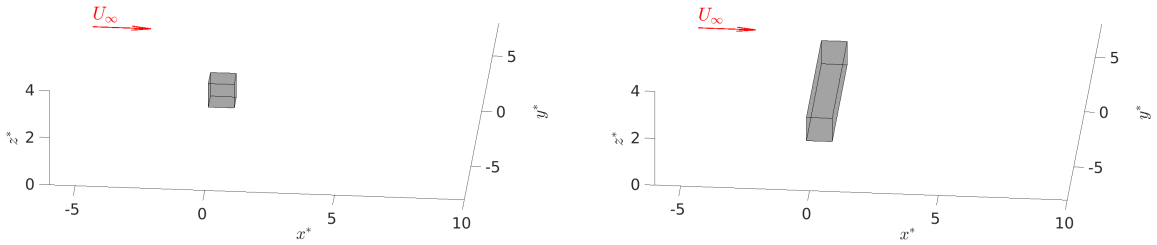

(a) *Cube* (b) *Cylinder*

Figure 3: Schematic representation of studied obstacles.

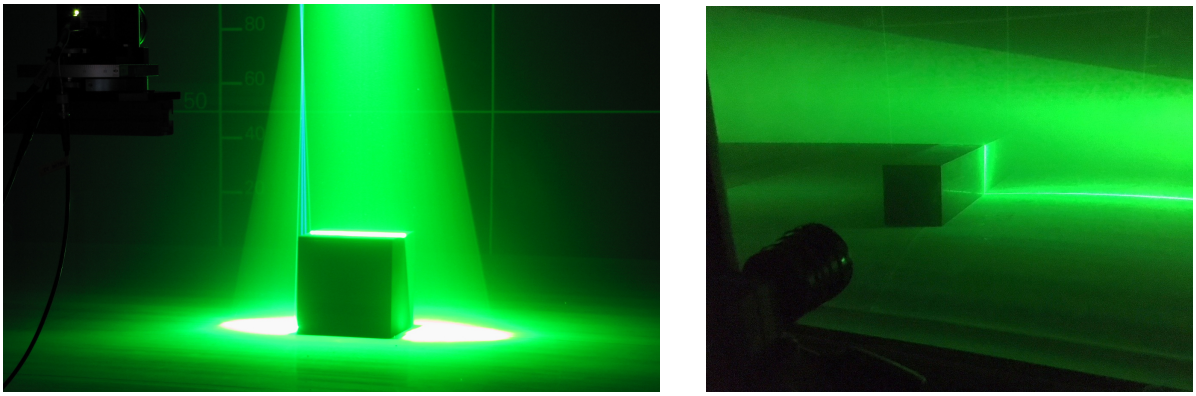

(a) The cube lighted with PIV laser sheet and LDV laser beams.

(b) The cylinder lighted with PIV laser sheet.

Figure 4: Pictures of obstacles in the tank.

peak detectability [Adrian, Westerweel (2011)] is 8 in average. PIV acquisitions are made for 150 s, hence 2250 double images are taken with a 15 Hz acquisition frequency. The data are post processed with DYNAMIC STUDIO. Particles displacement is calculated using a Cross-Correlation [Meinhart et al. (1993)]. Outliers are then replaced with the Universal Outlier Detection [Westerweel, Scarano (2005)]. Examples and details on that method can be found in [Ikhennicheu et al. (2019b)].

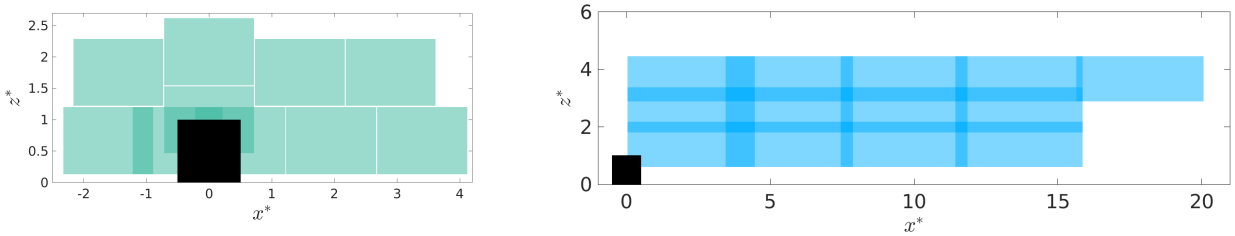

(a) (b)

Figure 5: PIV measurements planes locations in the symmetry plane for the cube (left) and cylinder (right) test cases.

Narrow-angle lens are used for cube case and wide-angle lens for the cylinder. Measurements fields are limited to 1600 $pixels \times 1200$ $pixels$ for the cube and 1600 $pixels \times 800$ $pixels$ for the cylinder, the laser lightens the symmetry plane and the camera is positioned beside the obstacle. The PIV measurement plane positions depend on the wake topology, which are illustrated in Figure 5 for both cases. Spatial discretisation is 3.53 mm for the cube and 11.6 mm for the cylinder.

The LDV measurements are performed using a 2D DANTEC FiberFLOW system. With LDV measurements, the acquisition frequencies are not constant. They depend on the occurrence of a particle passing through the measurement volume. At a given stream-wise position, f_e varies from 70 to 270 H_z depending on the turbulent agitation. LDV signals (duration of 6 minutes) are re-sampled with a fixed sampling frequency f_e [Duràn Medina et al. (2015)]. For each stream-wise position x^*, the lowest average f_e for each altitude is taken. Beforehand, fluctuating velocity signals are cut into blocs of 1024 points and a Fast Fourier Transform (FFT) is applied on every block. Then the Power Spectrum Density (PSD) averaged over these blocks is plotted versus the Strouhal number $S_t = fH/U_\infty$. For the two measurement techniques, uncertainty is estimated to be around 2% for LDV and 2.6% for PIV. Calculations are presented in details in [Ikhennicheu et al. (2019b)]. Results are exposed in [Ikhennicheu et al. (2018)], [Ikhennicheu et al. (2019b)] and [Ikhennicheu et al. (2019a)].

2.2. LBM-LES numerical methodology

LBM-LES numerical simulations are performed with the open source C++ library developed by Flowkit Ltd under the name Palabos. The collision operator is the BGK operator [Chen, Doolen (1998)] with a D3Q19 discretisation scheme. A regularisation procedure introduced by [Latt, Chopard (2006)] and improved by [Malaspinas (2015)] is used to increase numerical stability. The LES model in use is the static Smagorinsky sub-grid model. This model consists in modelling the dissipation of turbulent scales by increasing the fluid viscosity. It introduces the Smagorinsky constant that is set equal to 0.14. All boundary conditions are of type Dirichlet, based on the developments of [Zou, He (1997)]. The velocity at the bottom of the channel is defined through a law of the wall based on Spalding model [Launder, Spalding (1974)]. Considering the very low turbulence rate in the experimental case ($I = 1.5$ %), the inlet boundary condition is set to be constant in time, and uniform in the span-wise direction. The inlet vertical velocity profile is set equal to the time averaged profile measured in the experiment upstream of the wall-mounted obstacle. Geometries are defined with a no-slip Bouzidi off-lattice condition [Bouzidi et al. (2001)]. This condition consists in the interpolation of the fluid velocity on near wall grid nodes. The velocity on these nodes is set to be consistent with a zero velocity on the wall.

The simulation domain is divided into zones of different resolution. Due to the Cartesian nature of LBM grids, the mesh cell dimension is uniform within a same zone, and is divided or multiplied by a factor 2 between two adjacent zones. This constraint proscribes progressive mesh expansion ratio, which strongly complicates near-wall mesh refinement. Theoretically, an accurate LES simulation should use a fine mesh resolution in order to resolve strong velocity gradients in the viscous boundary layer. The computational resource available was not sufficient to satisfy this condition for simulations presented in this paper. Commonly, wall functions are used to overcome this issue. Wall functions are only valid under the hypothesis that the flow tends to be parallel to the wall. They are thus adapted to represent the bottom boundary condition, but inadequate on the macro roughness geometry. [Nikuradse (1950)] or [Perry et al. (1969)] showed that when the roughness dimension is higher than the viscous value (typically the thickness of the viscous sub-layer), the physics of the flow is not driven by viscosity any more. Thus, the condition for the mesh resolution to resolve viscous sub-layer gradients is not apropos. This will be verified through a mesh convergence procedure and the comparison to the experiments in the next sections.

2.3. Wavelet analysis

Wavelets are usually used to detect periodic characteristics of time series subjected to time-varying frequency. The main advantage of wavelets is to be localised in both time and frequency whereas the standard Fourier transform is only localised in frequency. In other words, a Fourier transform identifies frequencies that are present in the signal, whereas a wavelet transform identifies the time variation of the power carried by each frequency. Wavelet analysis had demonstrate its superiority over Fourier analysis

in cases such as unsteady signals [Akin (2002)] and when the numerical time duration is not sufficient to obtain converged Fourier results. The wavelet analysis is performed under the R language [R Core Team (2018)] using the *WaveletComp* package [Roesch, Schmidbauer (2018)] based on the Morlet mother wavelet [Morlet et al. (1982)].

2.4. Flow around a wall-mounted cube for numerical validation

A comparison between current flume tank experiments [Ikhennicheu et al. (2018)] and LBM simulations of a wall-mounted cube is performed. It aims to establish a reference case and to validate the LBM simulation tool. The geometry has small dimensions and induces a short wake, so it is less demanding in computational resources than larger geometries. It is thus adapted to define simulation parameters and to perform a mesh convergence.

2.4.1. Mesh resolution

The simulation domain, based on the tank depth and width, is 4 meters long, 4 meters wide and 2 meters high. The wall-mounted cube is placed 2 meters after the domain inlet. The mesh resolution is chosen through a mesh convergence procedure. This procedure is performed by adding finer mesh resolution zone around the cube. Figure 6 presents a longitudinal cut of three mesh types (named LBM100, LBM200 and LBM400) in which the cube is coloured in blue. Zones of different resolution are materialised by squares of different sizes. Each square's side is 12 mesh cell long. The size of the finest cells is 10.4 mm in Figure 6a, 5.2 mm in Figure 6b and 2.6 mm in Figure 6c. Simulations using these meshes are launched with a wake establishment period of 50 seconds followed by data acquisition and averaging during 80 seconds.

The error is estimated through two indicators, relative maximum error (see Equation 2) and relative mean square error (see Equation 3). The error on a given quantity X is normalised by a reference quantity X_{ref}. Here X_{ref} is chosen equal to U_∞ for velocity components and to the maximum value of $\overline{u'u'}$ for the velocity component variance. Comparison between meshes is performed on vertical profiles of averaged longitudinal velocity, in the wake of the cube, for three different distances from the cube and for the three mesh types. Graph comparison is showed in Figure 7 and numerical error results are summed up in Table 2. Profiles taken from LBM400 simulation are far from LBM200 simulation, with a relative mean square error of 9.3% and a relative maximum error of 27%. This demonstrates that the LBM400 resolution is not sufficient to simulate physical phenomena involved in this case. By contrast, LBM100 and LBM200 show a good agreement, with a relative mean square error of 1.8% and a relative maximum error of 6.7%. Mesh convergence is thus considered to be achieved with the LBM200 mesh. This resolution is hereby chosen for all the calculations in the scope of this work.

$$MaxError(X) = \frac{max(X - X_{exp})}{X_{ref}} \tag{2}$$

$$MeanSquareError(X) = \frac{\sqrt{\int_\Omega \frac{(X-X_{exp})^2}{L} d\omega}}{X_{ref}} \tag{3}$$

	LBM200 vs LBM400	LBM100 vs LBM200
Relative mean square error	9.3 %	1.8 %
Maximum relative error	27 %	6.7 %

Table 2: $\overline{U}$ error evaluation between simulations using different meshes in the case of a wall-mounted cube. The error is averaged over the vertical profiles presented in Figure 7, in the symmetry plane $y^* = 0$

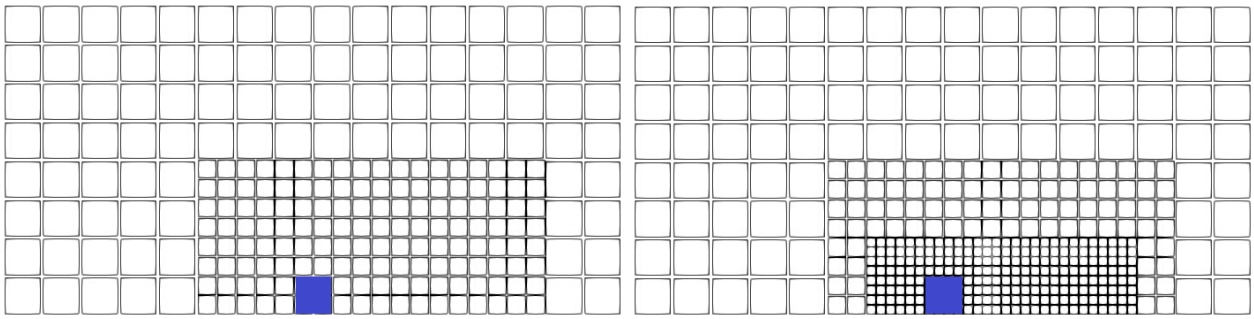

(a) LBM 400.

(b) LBM 200.

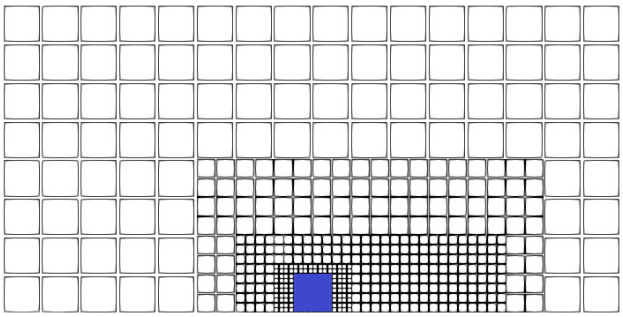

(c) LBM 100.

Figure 6: Meshes used for mesh convergence study. Each square's side is 12 mesh cell long.

2.4.2. Results

Time averaged data from numerical simulations are compared to experiments. Figure 8 presents vertical time averaged profiles downstream of the cube. Longitudinal and vertical velocity components appear respectively in Figure 8a and Figure 8b. Three vertical profiles are plotted for each velocity component, at a distance downstream of the centre of the cube of 1H, 2H and 3H. Figure 8c, Figure 8d and Figure 8e illustrate $\overline{u'u'}$, $\overline{w'w'}$ and $\overline{u'w'}$ respectively, $1H$ downstream of the cube. These simulation profiles are similar to PIV experiments.

Relative errors between simulations and experiments are evaluated for the vertical profile situated at a 1H distance downstream of the cube and results are summed up in Table 3. The relative mean square error is limited to 5 %, while the maximum error is less than 5% for averaged velocity components and reaches a maximum of 12 % for averaged velocity variance components. These values are acceptable considering the experimental uncertainty.

Hence, the simulation results fit well the PIV measurements. These good agreements obtained with a quite coarse mesh tend to validate the assumption that viscous effects are negligible compared to the effect of the macro-roughness. They suggest that the model is able to reproduce dominant physical phenomena. No remarkable vortex emission is observed in the wake of the wall-mounted cube, like in the experimental investigation. This leads to the study of another macro-roughness geometry in the next section.

	$\overline{U}$	$\overline{W}$	$\overline{u'u'}$	$\overline{w'w'}$	$\overline{u'w'}$
Relative mean square error	3.9 %	1.5 %	5.1 %	4.1 %	1.4 %
Relative max error	4.5 %	3.2 %	12 %	11 %	5.1 %

Table 3: Error evaluation between simulation and experiment in the case of a wall-mounted cube ($x^* = 1$).

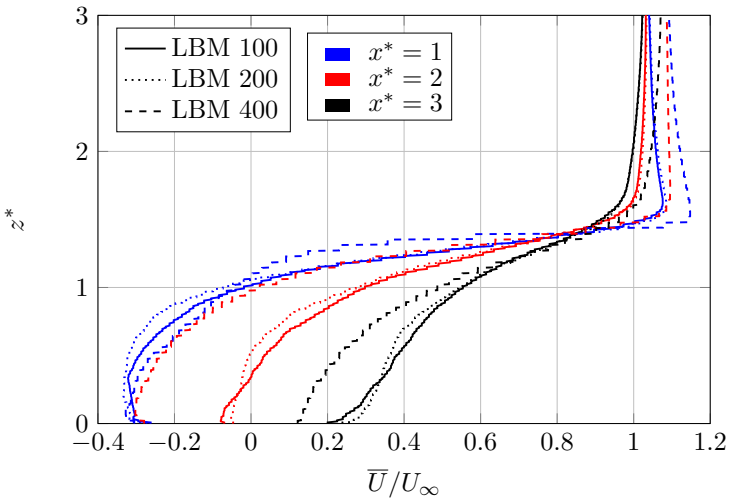

Figure 7: Mesh convergence of the cube simulation case for three mesh types. Vertical profiles of time averaged longitudinal velocity, $y^* = 0$.

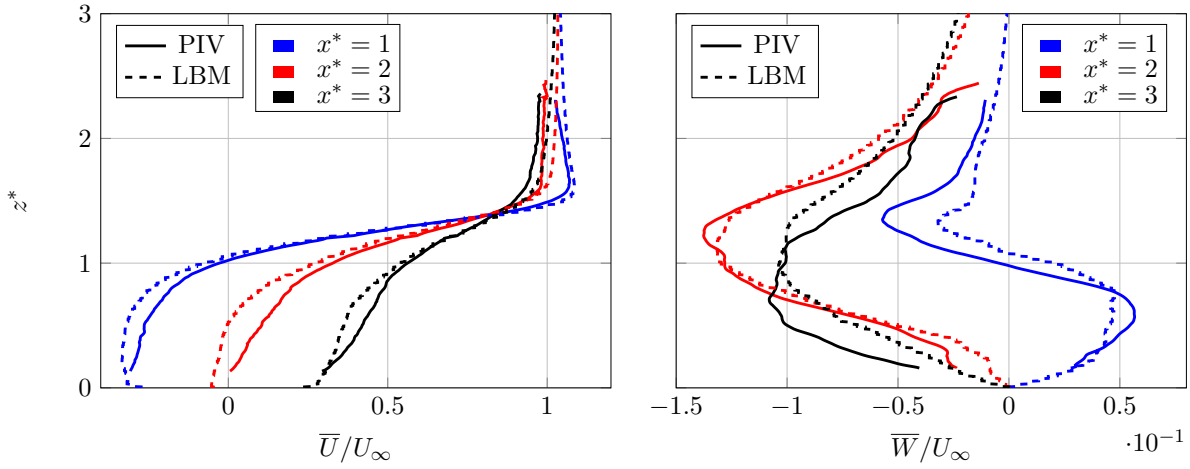

(a) Normalised averaged longitudinal velocity.

(b) Normalised averaged vertical velocity.

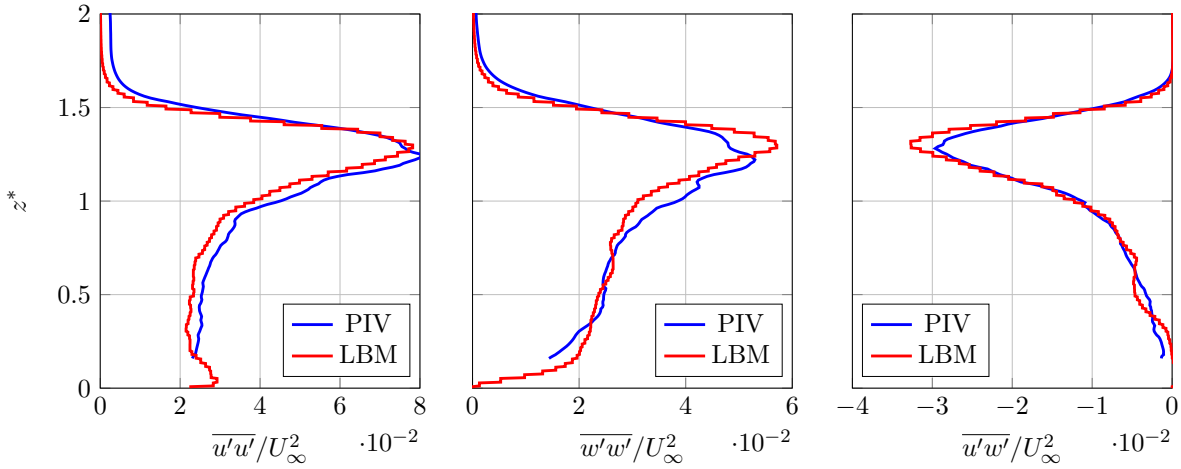

(c) Normalised variance of longitudinal velocity component.

(d) Normalised variance of vertical velocity component.

(e) Normalised covariance of longitudinal and vertical velocity components.

Figure 8: Comparisons between numerical simulation and experiment [Ikhennicheu et al. (2018)] of time averaged vertical profiles velocity and velocity variance downstream of a wall-mounted cube.

3. Characterisation of the vortices emitted in the wake of a wall-mounted cylinder

The experimental case of a wall-mounted cylinder led to the observation of boils in the cylinder wake and was described in [Ikhennicheu et al. (2019b)] and [Ikhennicheu et al. (2019a)]. The characterisation of the dynamic behaviour of the vortices shed from the obstacle can only be partially covered from 2D PIV measurements. By using numerical simulation, we complement this study with pressure measurements, tracking of instantaneous events on the whole domain of study and three-dimensional data.

The domain is 2 m high, 4 m wide and 16 m long. The mesh resolution is based on the previous section results. The mesh contains 52.2 million nodes. The simulation lasted 48 hours on 112 processors, resulting in a simulated time of $t^* = 720$. No data is acquired during $t^* = 240$ (the duration required to obtain a fully developed wake). Then average calculus starts. Reynolds tensor components are calculated using velocity average obtained at $t^* = 480$.

Time-averaged simulation results are compared to the experimental measurements. Figure 9 presents comparisons on a vertical profile situated downstream of the cylinder, at a 1H distance from the cylinder centre. A quantitative estimation of the difference between numerical simulation and experiment is also given in Table 4. On this profile, averaged longitudinal velocity and longitudinal velocity variance show higher discrepancy ranging from 7% to 9% for the relative mean square error and between 26% and 34% for the relative maximum error. Although errors are greater than those obtained for the cubic macro-roughness case, these values are acceptable because, as illustrated in Figure 9a and Figure 9b, they are mostly imputed to a vertical shift of the profiles. Indeed, the shapes and extreme values on both graphs show a good agreement between numerical simulation and experiment. The simulation is thus considered to properly simulate the experimental case and is then further developed to investigate the behaviour of the turbulent flow.

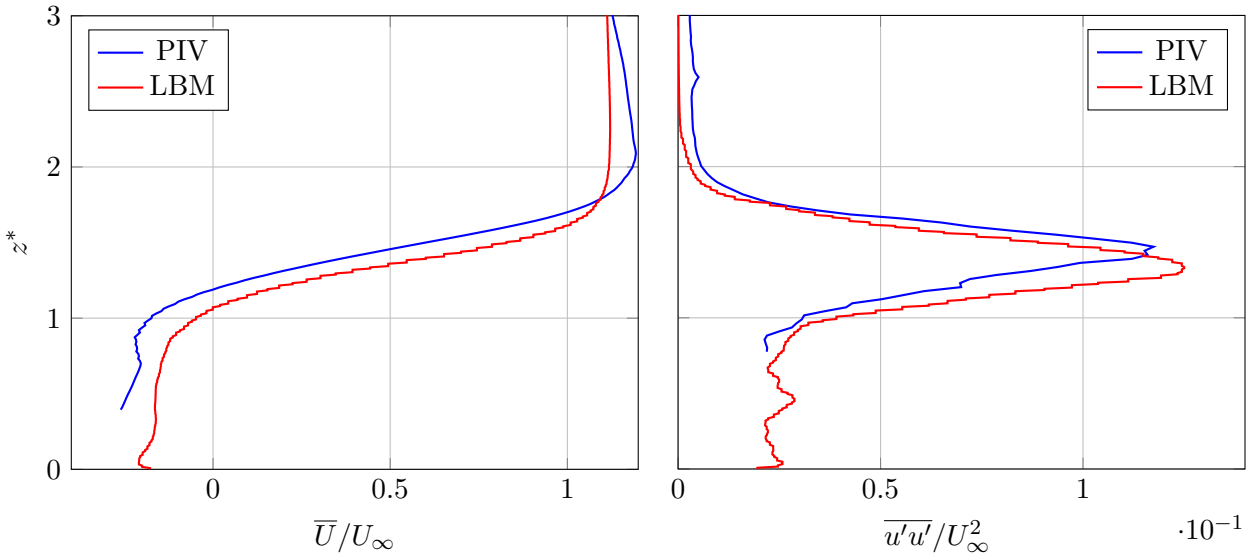

(a) Normalised averaged longitudinal velocity.

(b) Normalised variance of longitudinal velocity.

Figure 9: Comparison between experimental [Ikhennicheu et al. (2019b)] and numerical results on vertical profiles situated 1H downstream of a wall-mounted cylinder.

3.1. Qualitative analysis of turbulent flow structures

The numerical simulation allows the use of visualisation tools to identify physical phenomena occurring in the cylinder wake. These tools require heavy data and post-processing that limit their intensive

	$\overline{U}$	$\overline{uu}$
Relative mean square error	9.0 %	7.6 %
Relative max error	26 %	34 %

Table 4: Error evaluation between simulation and experiment in the case of a wall-mounted cylinder.

use. However, as the simulation is deterministic, it is possible to identify interesting phenomena from sparse data extracted from the simulation and then launch the simulation again at the selected period when extensive data is requested. This study aims to identify the process involved in the generation of large vortices downstream of the cylinder, as identified in [Ikhennicheu et al. (2019b)]. The creation of Kelvin-Helmholtz vortices is promoted here and their behaviour is specifically investigated.

3.1.1. General structure of the flow

Figure 10 presents the general structure of the flow through $lambda_2$ criterion isosurface plotting [Jeong, Hussain (1995)]. The cylinder is situated in the down left corner and the flow comes from the left. A large vortex structure is visible in the far wake. This structure is well separated from the rest of the cylinder wake. Its size is of the order of magnitude of the cylinder width. In the closer wake, composed of small vortex structures, another large vortex structure is emerging. It consists in a mixing of medium size hairpin vortices. The trajectory of these large structures is consistent with the experimental results of [Ikhennicheu et al. (2019a)] in Figure 11, which shows the numerical model capacity to simulate their dynamic. The lateral extremities of the cylinder leading edge is exempt of turbulent events. On the central part, turbulent events pass over the leading edge.

The next visualisations focus on specific areas represented with black frames in Figure 12. This figure introduces velocity vectors coloured by span-wise vorticity in the cylinder symmetry plan. Zone 1 is situated in the immediate wake of the cylinder and allows the observation of coherent flow structures formation. Their early intern evolution is observed in Zone 2, a bit further in the cylinder wake. Their late evolution is investigated within Zone 3 and Zone 4, further and higher in the wake.

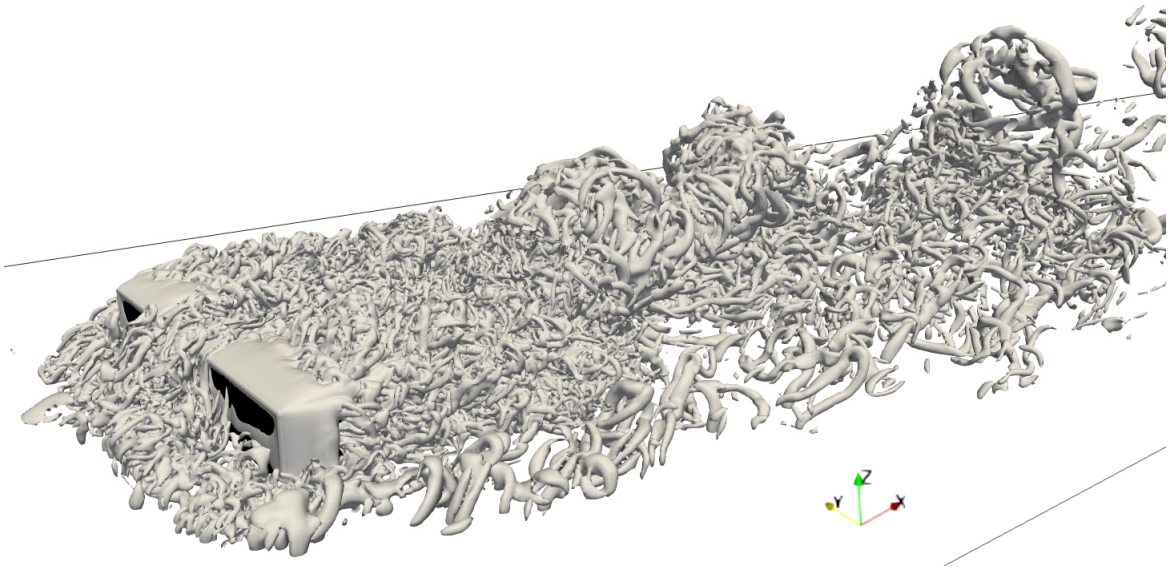

Figure 10: $lambda_2$ criterion visualisation of turbulent motions downstream of a wall-mounted square cylinder. A movie is available at this link: "Movie1".

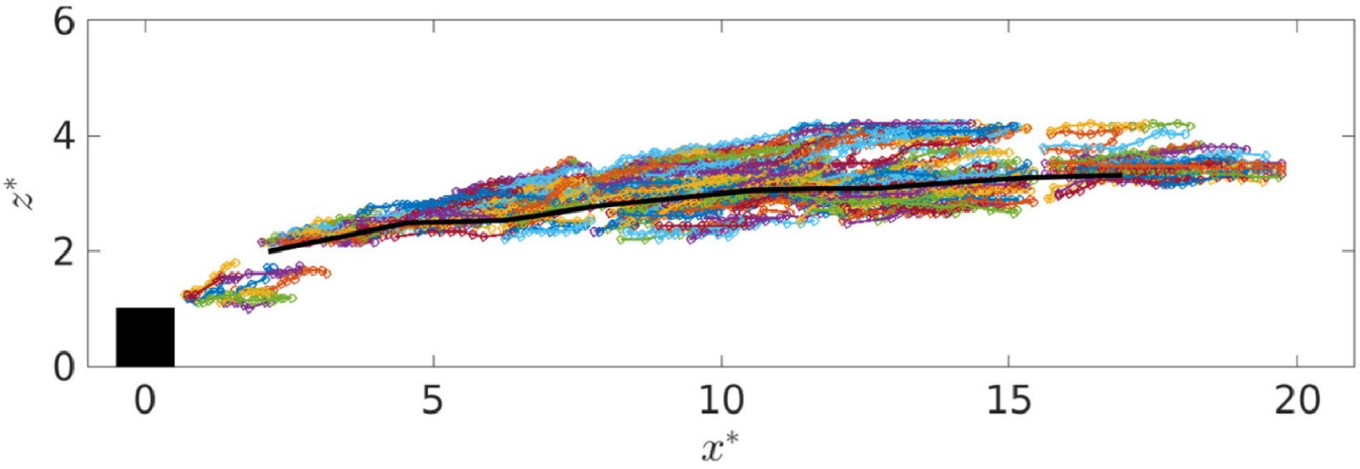

Figure 11: Vortex trajectories in the symmetry plane of a wall-mounted cylinder. The black line stands for the top of the shear layer. Experimental case conducted by [Ikhennicheu et al. (2019a)].

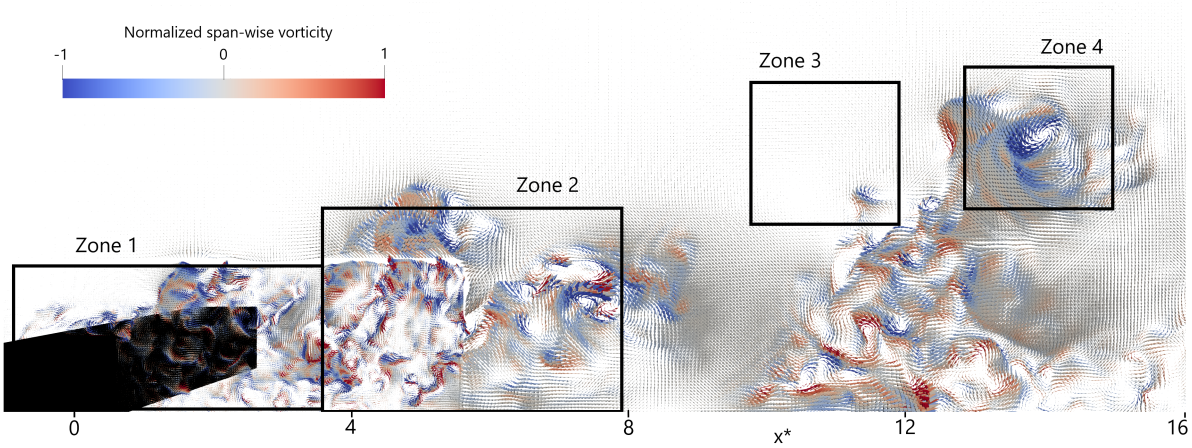

Figure 12: Visualisation of the wake of a wall-mounted cylinder in the symmetry plane through velocity vector plotting coloured by normalised span-wise vorticity.

3.1.2. The aggregation of Kelvin-Helmholtz vortices into a coherent flow structure

Vortex structures regularly form at the trailing edge of the cylinder. They are very similar to classical Kelvin-Helmholtz vortices described in [Comte et al. (1998)]. The early stage of these vortices is presented in Figure 13 with $lambda_2$ criterion isosurface plot. They consist in rolls stretched in the span-wise direction. Their span-wise dimension is of the order of magnitude of the cylinder width. They seem to form and detach simultaneously along the whole cylinder width. The frequency of emission is estimated around $St = 1$ through video visualisation. The emission seems to be regular. However, the visualisation period is too short ($t^* = 8$) to extrapolate a general behaviour from this observation.

Longitudinal cut of pressure contours downstream of the cylinder, on Zone 1, were extracted at a $St = 5$ frequency. A succession of such picture is presented in Figure 14, spaced by a $t^* = 1$ time ($St = 1$ frequency). Interstitial pictures can be found in the movie accessible through the link in Figure 14 caption. Blue colour denotes low-pressure zones, namely rotation centres, and red colour denotes high-pressure zones. In Figure 14a, one vortex is already detached from the cylinder trailing edge, and another one is about to detach. In Figure 14b, these two vortices have merged into a larger one. Then vortices continue detaching from the cylinder trailing edge and merging into the growing aggregate of turbulent

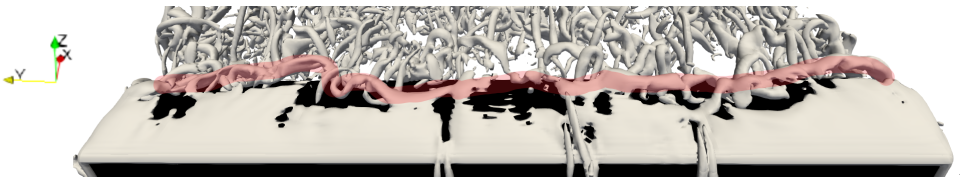

Figure 13: $lambda_2$ visualisation of a Kelvin-Helmholtz vortex (coloured in red) at the trailing edge of a wall-mounted cylinder.

motions, as illustrated in Figure 14c to Figure 14g. The aggregate stays immediately downstream of the cylinder. Figure 14h to Figure 14j show that the aggregate detaches from the cylinder and is followed by new small vortices. It is then transported in the wake of the cylinder. This shows that large vortex structures downstream of the cylinder may be generated through aggregation of smaller vortex structures emitted at the trailing edge of the cylinder. The pairing of vortices, that has been widely described in the literature for two vortices ([Chandrsuda et al. (1978)], [Müller, Gyr (1986)]), is here observed with higher number of Kelvin-Helmholtz vortices.

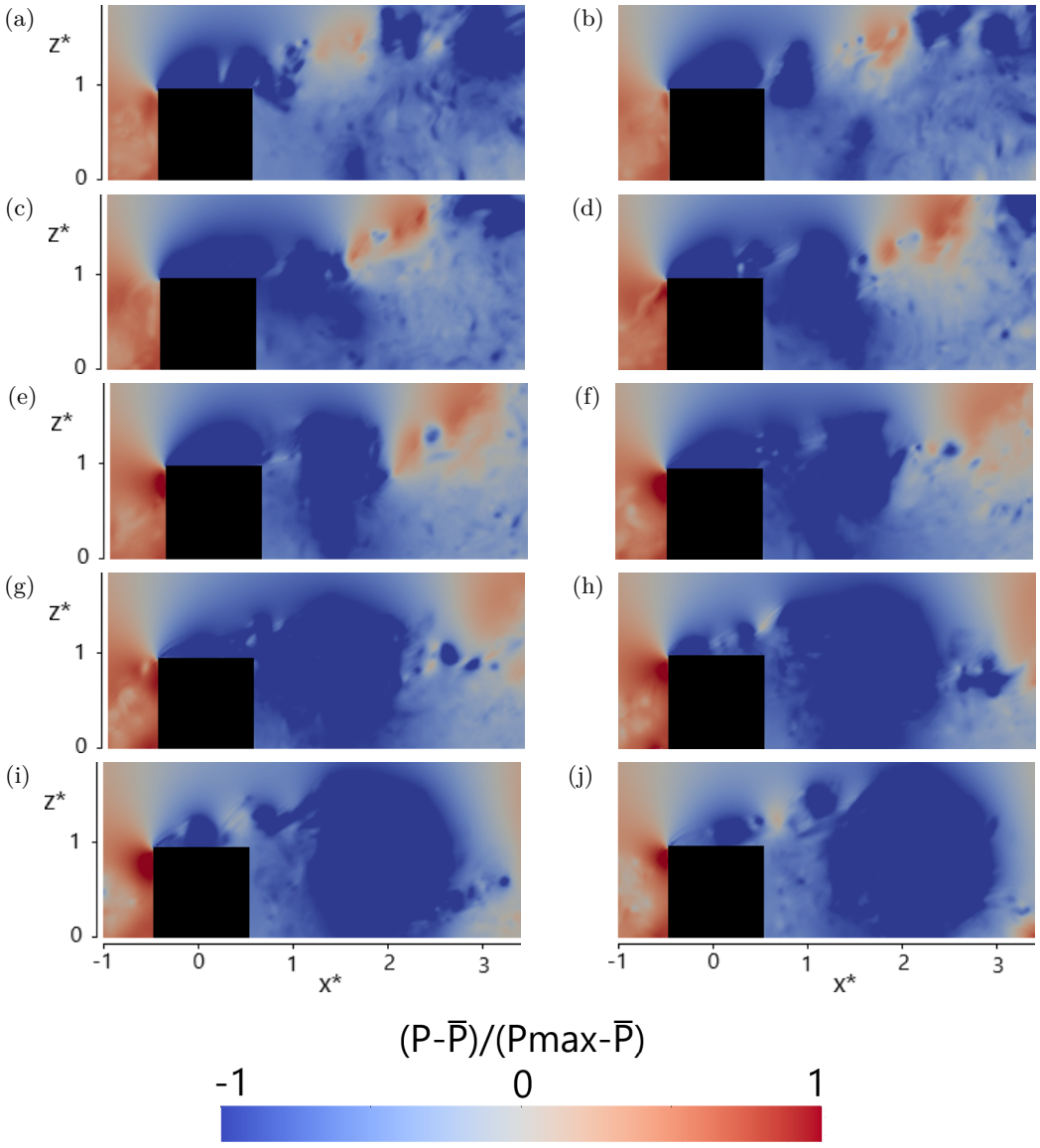

Figure 14: Aggregation of Kelvin-Helmholtz vortices downstream of a wall-mounted cylinder. Fluctuating pressure field visualisation. Low-pressure area are coloured in blue, high pressure in red. A movie is available at this link: "Movie2".

3.1.3. The inside dynamic of a coherent flow structure

Three-dimensional $lambda_2$ criterion isosurface plotting is performed in Zone 2 to assess the inside dynamic of a coherent flow structure formed by aggregation of Kelvin-Helmholtz vortices. The snapshots represented in Figure 15 are obtained by a longitudinal cut removing half of the domain.

Three Kelvin-Helmholtz vortices are identified in Figure 15a. They are regularly spaced. The first one, identified with a blue dot, initiates a downward trajectory in a re-circulation overall movement. It is followed by two vortices identified with red and green dots. Their dynamics can be followed on the next pictures. In Figure 15b, the red vortex is caught in the re-circulation movement. The three vortices rotate around each other (Figure 15c and Figure 15d). This rotating trend turns to an upward motion of the blue and green vortices (Figure 15e and Figure 15f) in which the red vortex is not taken. The blue and green interacting vortex structures are ejected from the agitated cylinder wake and form a larger and more complex vortex structure.

This time tracking confirms that the turbulent motions interact to shape larger vortex structures and suggests that they keep their physical integrity. Large coherent flow structures observed downstream of the cylinder are thus highly dependent on the individual vortices they contain, which highlights the necessity to properly track small turbulent motions to understand the behaviour of larger motions.

In the experimental study, coherent flow structure tracking showed large turbulent structures with a unique rotation centre [Ikhennicheu et al. (2019b)]. Velocity vectors field visualisation is performed to investigate the formation mechanism of such structures. In Figure 16, velocity vector fields are plotted in the cylinder symmetry plane and coloured with span-wise vorticity. Blue colour stands for clockwise rotation whereas the red represents anti-clockwise rotation. The two images picture the same coherent flow structure one second apart, in Zone 3 and Zone 4 respectively. In Figure 16a, velocity vector directions highlight the overall clockwise rotational motion. Three distinct clockwise rotation centres are identified. They denote that three vortices are organised in a braid and form the coherent flow structure. Figure 16b pictures the same structure one second later. During this period, the three distinct centres merged to form a unique clockwise rotation centre. Localised rotational motions combined to give an overall an uniform rotational behaviour to a large coherent flow structure.

This observation confirms that large coherent flow structures are created by the merging of smaller vortices having the same rotating motion. The characteristics of coherent flow structures observed in the experiment may thus be linked to the Kelvin-Helmholtz vortices generated at the trailing edge of the cylinder.

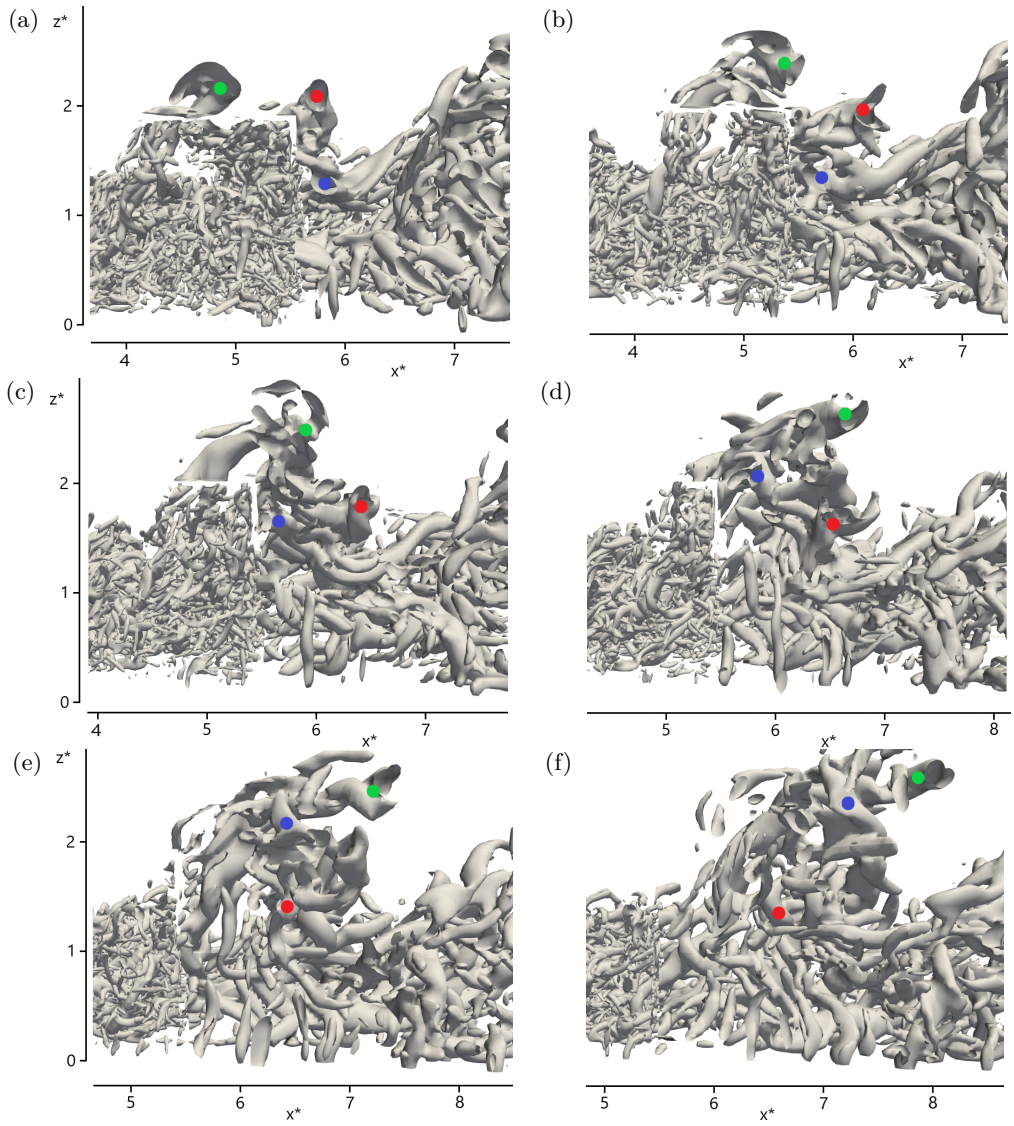

Figure 15: Interaction of Kelvin-Helmholtz vortices within a coherent flow structure. Lambda 2 visualisation. A movie is available at this link: "Movie3".

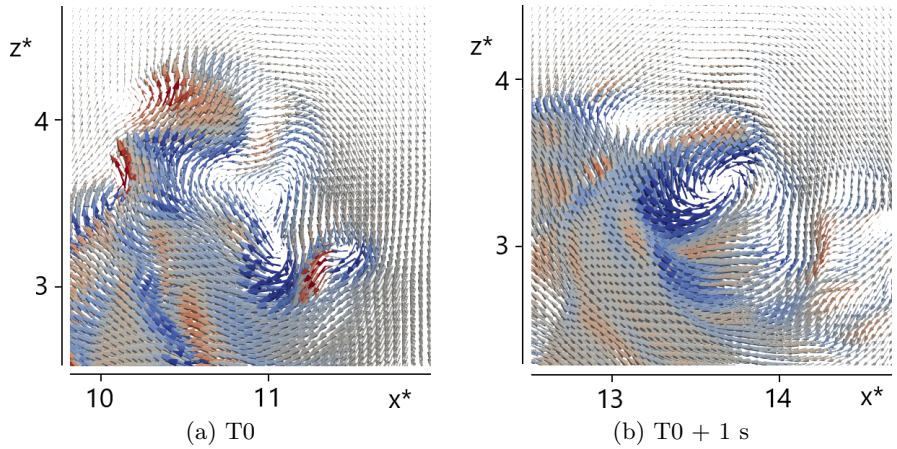

(a) T0 (b) T0 + 1 s

Figure 16: Coherent flow structure composed of three rotation centres merging into one. Velocity fluctuation vectors coloured by span-wise vorticity. Blue areas stand for clockwise rotation, red areas for anti-clockwise rotation.

3.2. Spectral analysis

Due to computational constraints and the huge data required for visualisation, only a limited number of vortex structures have been visualised. Thus, the observed phenomena cannot be assessed to be generic. Visualisation study showed cyclic phenomena such as the successive emission of Kelvin-Helmholtz vortices and the successive emission of coherent flow structures. To investigate if these phenomena are systematic and regular, a frequency analysis is necessary. It only requires punctual data and can thus be performed on a longer period than visualisation.

Frequency analysis is conducted on long data sample to investigate the regularity of cyclic turbulent events. The experimental study showed the appearance of an energy peak for frequencies around $St = 0.07$ [Ikhennicheu et al. (2019b)]. A comparison between spectra from experiment and numerical simulation at points situated at $x^* = 7$ is presented in Figure 17. The numerical simulation detects the same energy peak and the energy distribution is similar to the experiment. This low frequency peak around $St = 0.07$ is associated with the emission of large-scale coherent flow structures. No energy peak is identified at higher frequency. This suggests that the energy carried by the Kelvin-Helmholtz vortices, that are suspected to be released at frequencies around $St = 1$, has been transferred to other frequencies before reaching $x^* = 7$.

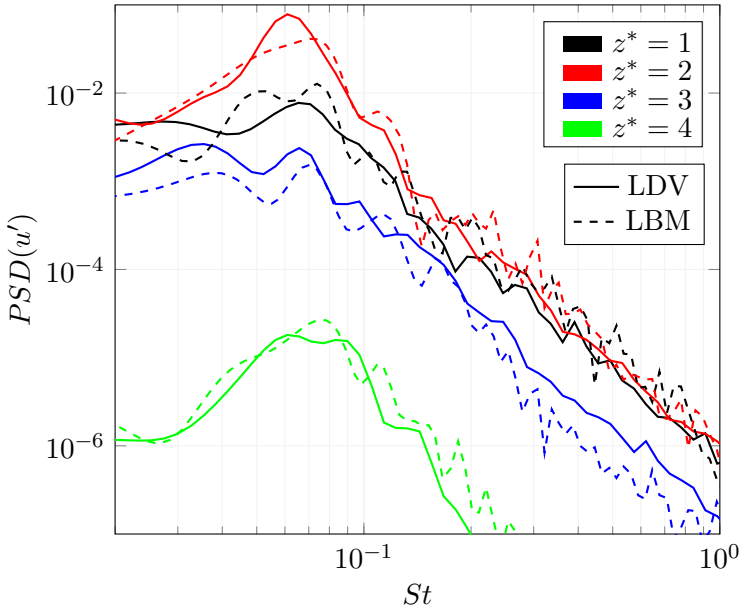

Figure 17: Comparison between numerical and experimental results of power spectral density of longitudinal velocity fluctuations in the wake of a wall-mounted cylinder at $x^* = 7$.

Spectral analysis is also conducted at the trailing edge of the cylinder to identify the frequency of Kelvin-Helmholtz vortices emission. The probe coordinates are (0.5H; 0; 1.25H). Despite visualisation of regularly emitted vortices, no energy peak was detected in the Fourier transform analysis. However, velocity signal plotting shows cyclic events in Figure 18. Three different periods, from $t^* = 587$ to $t^* = 598$, from $t^* = 598$ to $t^* = 606$ and from $t^* = 606$ to $t^* = 616$ suggest the occurrence of cyclic events. The first period is characterised by high amplitude, smooth and slow variations, the second period by low amplitude variations at a very high frequency and the third period by moderate amplitude and moderate frequency variations. A wavelet study is then conducted to investigate the frequency variability of turbulent events at the probe position.

The wavelet power spectrum of vertical velocity is computed. It is represented in terms of isosurface

in Figure 19 for a 110 second sample. The x axis stands for time and the y axis stands for the frequency of turbulent events. The highest wavelet coefficients are coloured in black to better identifying the most energetic structures. Most of the energetic frequencies range between $St = 0.125$ and $St = 2.5$. However, the width of the black spots is restrained to some seconds, and the spots are not centred on a specific frequency. This suggests that various patterns of Kelvin-Helmholtz vortices emission follow one another, during short periods and on different frequencies.

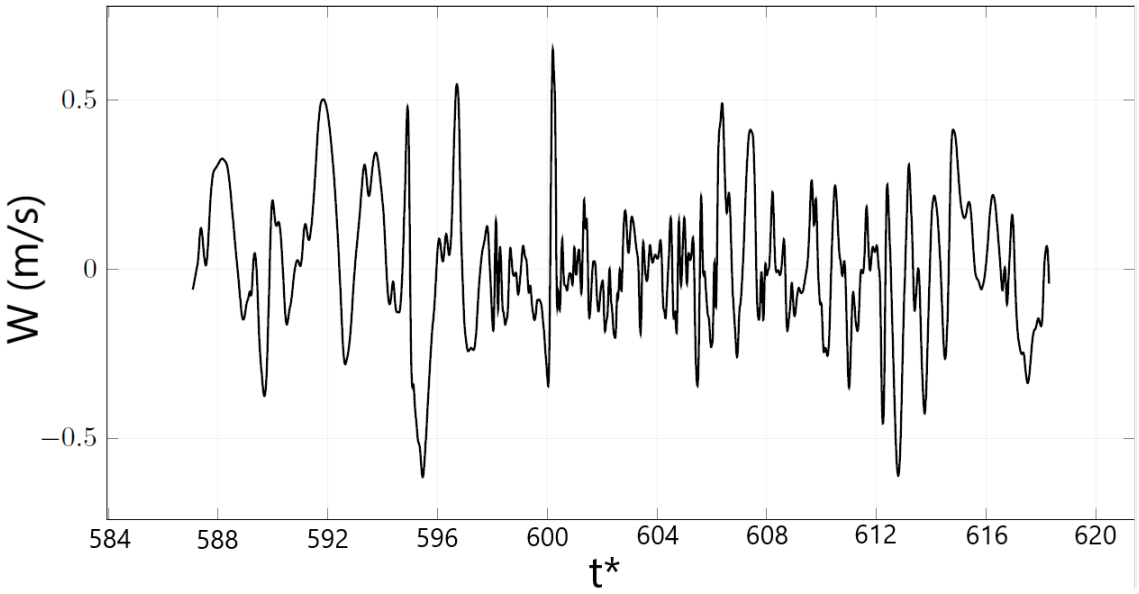

Figure 18: Time series of vertical velocity component at the trailing edge of a wall-mounted cylinder at (0.5H; 0; 1.25H).

Figure 20 corresponds to the time-averaged power spectrum. It allows identifying the frequencies with the greatest power. In addition, the red dots highlight sections of the signal with significant recognised periodicity. The result is a statistical test performed during the wavelet transform computation and expressed as a p-value. As previously illustrated in the wavelet power spectrum figure, most of the power is localised between $St = 0.25$ and $St = 2$. It is regularly distributed within this range of frequency. Despite two peaks are observed at $St = 0.59$ and $St = 1.0$, they are not significant enough to overshadow the fact that the power is distributed over this wide range of frequencies. This confirms the assumption that there is no specific frequency associated with the emission of Kelvin-Helmholtz vortices downstream of the wall-mounted cylinder. This emission frequency varies in time and is only stable over short periods. Thus, it cannot be detected on spectra.

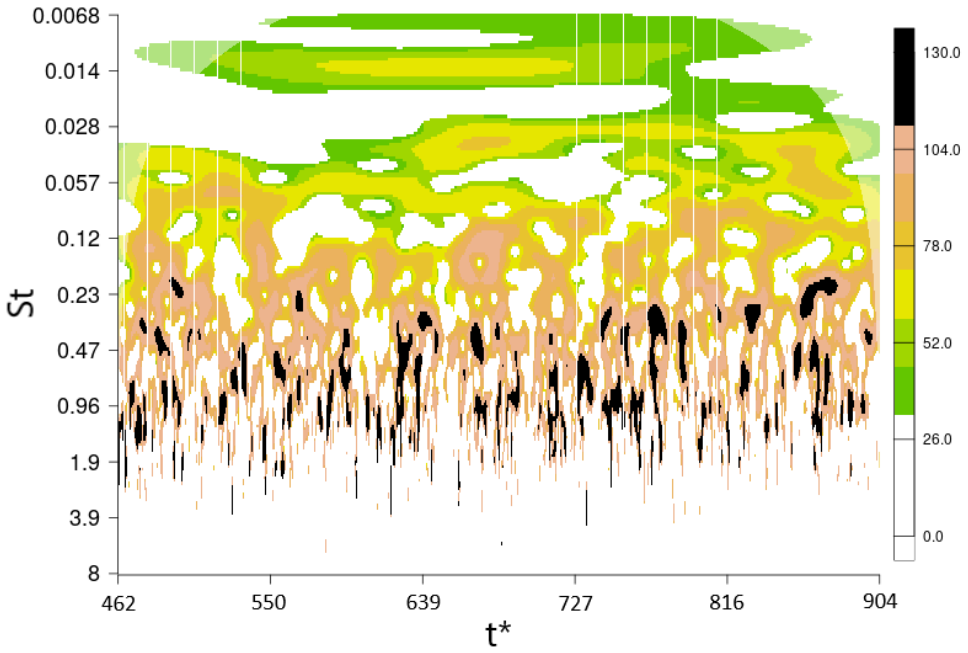

Figure 19: Wavelet power spectrum of the vertical component of the flow velocity data set at the trailing point edge of a wall-mounted cylinder at (0.5H; 0; 1.25H).

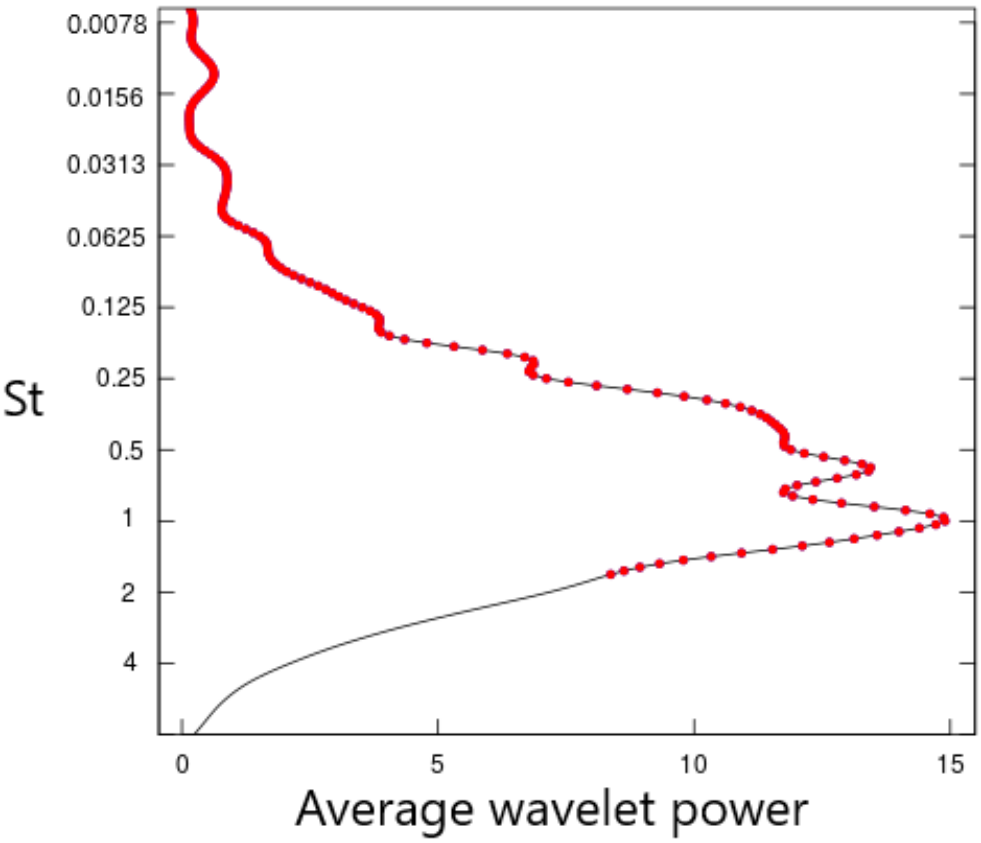

Figure 20: Average wavelet power of the vertical component of the flow velocity data set at the trailing point edge of a wall-mounted cylinder at (0.5H; 0; 1.25H).

4. Conclusion

LBM-LES numerical simulations of flows around wall-mounted macro-roughness have been performed. Simulation parameters have been validated by comparison with experimental measurements. Three-dimensional visualisation given by the numerical model offered a meaningful way to observe physical phenomena involved in the wake of a wall-mounted obstacle. The access to exhaustive data and the ability to relaunch simulation on selected period allowed to detect and track precisely turbulent motions.

In particular, large coherent flow structures observed in experiments have been studied in the case of a wall-mounted cylinder. They appeared to be formed through the aggregation of multiple smaller turbulent structures. These structures have been identified as Kelvin-Helmholtz vortices released at the trailing edge of the cylinder and aggregated downstream of the obstacle. Despite their aggregation into a larger turbulent motion, they kept their physical unity and interacted. The merging of three of these turbulent structures into a larger size vortex structure with a well defined rotational centre is observed.

However, due to the high variety of observed phenomena and the short period investigated through visualisation method, it is hard to propose a whole and unique process for the evolution of turbulent motions in the wake of a wall-mounted cylinder. In particular, the Kelvin-Helmholtz vortex release frequency varies in time and is only stable over short periods. This variability and the fact it does not affect the frequency emission of large-scale coherent structures has yet to be understood with further analysis.

The ability of the numerical tool to reproduce physical phenomena involved in the wake of a bed macro-roughness at high Reynolds number and with a coarse mesh is promising. This work will be used as a basis for the simulation of tidal flows over a real bathymetry. A special focus will be put on the emission of large coherent structures through process described in this article. Another perspective is the addition of a turbine model downstream of the cylinder to investigate the effect of large coherent flow structures on the turbine loads, like experimentally proposed in [Gaurier et al. (2019)].

Acknowledgement

This work benefits from a France Energies Marines and French State grant managed by the National Research Agency under the Investments for the Future program bearing the reference ANR-10-IEED-0006-11. The authors also acknowledge the financial support of Ifremer, the Hauts de France Regional Council for these PhD studies and CD50 for a postdoc position financing. We are grateful to the French navy SHOM ("Service Hydrographique et Océanographique de la Marine") for providing access to bathymetric data (http://data.shom.fr/). We are most grateful to Thomas Bacchetti, Inès Belarbi, Benoit Gaurier and Jean-Valery Facq for their assistance and precious advices.

References

Adrian R.J., Westerweel J. Particle Image Velocimetry // Cambridge University Press, Cambridge. 2011. 2.1

Akin M. Comparison of Wavelet Transform and FFT Methods in the Analysis of EEG Signals // Journal of Medical Systems. Jun 2002. 26, 3. 241–247. 2.3

Anderson W., Li Q., Bou-Zeid E. Numerical simulation of flow over urban-like topographies and evaluation of turbulence temporal attributes // Journal of Turbulence. 2015. 16. 809–831. 1

Best J. The fluid dynamics of river dunes: A review and some future research directions // J. Geophys. Res. 2005. 110. 1

Bhatnagar P.L., Gross E.P., Krook M. A model for collision processes in gases // Physical Review. 1954. 94, 3. 1

Bouzidi M., Firdaouss M., Lallemand P. Momentum transfer of a Boltzmann-lattice fluid with boundaries // Physics of Fluids. 2001. 13, 3452. 2.2

Castro I.P., Robins A.G. The flow around a surface-mounted cube in uniform and turbulent streams // Journal of Fluid Mechanics. 1977. 79. 307–335. 1

Chandrsuda C., Mehta R.D., Weir A.D., Bradshaw P. Effect of free-stream turbulence on large structure in turbulent mixing layers // Journal of Fluid Mechanics. 1978. 885. 693–7044. 1, 3.1.2

Chen S., Doolen G.D. Lattice Boltzmann method for fluid flows // Annual Review for Fluid Mechanics. 1998. 30. 329–364. 2.2

Cimarelli A., Leonforte A., Angeli D. Direct numerical simulation of the flow around a rectangular cylinder at a moderately high Reynolds number // Journal of Wind Engineering and Industrial Aerodynamics. 2018. 174. 39–49. 1

Coceal O., Dobre A., Thomas T.G. Unsteady dynamics and organized structures from DNS over an idealized canopy // International Journal of Climatology. 2007. 27. 1943–1953. 1

Comte P., Silvestrini J.H., Bégou P. Streamwise vortices in large-eddy simulations of mixing layers // European Journal of Mechanics - B Fluids. 1998. 17. 615–637. 1, 3.1.2

Diabil H.A., Li X.K., Abdalla I.E. Coherent structures and flow topology of transitional separate-reattached flow over two and three dimensional geometrical shapes // AIP Conference Proceedings. 1872, 020019. 2017. 1

Duràn Medina O., Schmitt F.G, Calif R., Germain G., Gaurier B. Correlation between synchronised power and flow measurements, a way to characterize turbulent effects on a marine current turbine // EWTEC. 2015. 2.1

Duràn Medina O., Schmitt F.G, Calif R., Germain G., Gaurier B. Turbulence analysis and multiscale correlations between synchronized flow velocity and marine turbine power production // Renew. Energ. 2017. 112. 314–327. 1

EDF . Énergies Marines hydrolienne et houlomotrice // Conférence institut Coriolis. 2010. 1

Florens E., Eiff O., Moulin F. Defining the roughness sublayer and its turbulence statistics // Exp Fluids. 2013. 54. 1500. 1

Gaurier B., Ikhennicheu M., Germain G., Druault P., Pinon G. Experimental study of the wall-mounted cylinder wake effect on tidal turbine behaviour compared to free stream turbulence // 13th European Wave and Tidal Energy Conference. 2019. 4

Hardy R.J., Best J.L., Parsons D.R., Marjoribanks T.I. On the evolution and form of coherent flow structures over a gravel bed: Insights from whole flow field visualisation and measurement // Journal of Geophysical Research: Earth Surface. 2016. 121. 1472–1493. 1

Ikhennicheu M., Gaurier B., Druault P., Germain G. Experimental analysis of the floor inclination effect on the turbulent wake developing behind a wall mounted cube // European Journal of Mechanics - B Fluids. 2018. 72. 340–352. 2.1, 2.4, 8

Ikhennicheu M., Germain G., Druault P., Gaurier B. Experimental investigation of the turbulent wake past realistic seabed elements for velocity variations characterisation in the water column // International Journal of Heat and Fluid Flow. 2019a. 78, 108426. 2.1, 3, 3.1.1, 11

Ikhennicheu M., Germain G., Druault P., Gaurier B. Experimental study of coherent flow structures past a wall-mounted square cylinder // Ocean Engineering. 2019b. 182. 137–146. 2.1, 2.1, 3, 9, 3.1, 3.1.3, 3.2

Jeong J., Hussain F. On the identification of a vortex // Journal of Fluid Mechanics. 1995. 285. 69–94. 3.1.1

Kwoll E., Venditti J.G., Bradley R.W., Winter C. Observations of coherent flow structures over sub-aqueous high- and low- angle dunes // Journal of Geophysical Research: Earth Surface. 2017. 122. 2244–2268. 1

Latt J., Chopard B. Lattice Boltzmann method with regularized pre-collision distribution functions // Mathematics and Computers in Simulation. 2006. 72. 165–168. 2.2

Launder B.E., Spalding D.B. The numerical computation of turbulent flows // Computer Methods in Applied Mechanics and Engineering. 1974. 3. 269–289. 2.2

Malaspinas O. Increasing stability and accuracy of the lattice Boltzmann scheme: recursivity and regularization // arXiv:1505.06900v1. 2015. 2.2

Matthes G.H. Macroturbulence in natural stream flow // Transactions, American Geophysical Union. 1947. 28, 2. 1

McMillan J., Hay A., Lueck R., Wolk F. An assessment of the TKE balance at a tidal energy site using ADCP and shear probe measurements // 12th European Wave and tidal Energy Conference (EWTEC). 2017. 1

Meinhart C.D., Prasad A.K., Adrian R.J. A parallel digital processor system for particle image velocimetry // Meas. Sci. Technol. 1993. 4. 619–626. 2.1

Morlet J., Arens G., Fourgeau E., Giard D. Wave propagation and sampling theory - Part II: Sampling theory and complex waves // Geophysics. 1982. 47. 222–236. 2.3

Müller A., Gyr A. On the vortex formation in the mixing layer behind dunes // Journal of Hydraulic Research. 1986. 24, 5. 1, 3.1.2

Mycek P., Gaurier B., Germain G., Pinon G., Rivolaen E. Experimental study of the turbulence intensity effects on marine current turbines behaviour. Part I: One single turbine // Renew. Energ. 2014. 66. 729–746. 1

Nikuradse J. Laws of flow in rough pipes. 1950. 2.2

Panigrahi P.K., Acharya S. Multi-modal forcing of the turbulent separated shear flow past a rib // Journal of Fluids Engineering. 2004. 126. 22–31. 1

Parmigiani A. A lattice Boltzmann simulation of the Rhone river // International Journal of Modern Physics C. 2013. 24, 12. 1

Perry A.E., Schofield W.H., Joubert P.N. Rough wall turbulent boundary layers // Journal of Fluid Mechanics. 1969. 37. 383–413. 2.2

Qian Y.H., D'Humières D., Lallemand P. Lattice BGK models for Navier-Stokes equation // Europhysics Letters. 1992. 17. 479–484. 1

R Core Team . R: A Language and Environment for Statistical Computing. Vienna, Austria, 2018. 2.3

Roesch A., Schmidbauer H. WaveletComp: Computational Wavelet Analysis. 2018. R package version 1.1. 2.3

MNT Bathymétrique de façade Atlantique (Projet Homonim). // . 2015. 1

Sagaut P. Large Eddy Simulation for Incompressible Flows. 2006. 1

Smagorinsky J. General circulation experiments with the primitive equations // Monthly Weather Review. 1963. 91, 3. 99–164. 1

Succi S., Foti E., Higuera F. Three-Dimensional Flows in Complex Geometries with the Lattice Boltzmann Method. // Europhysics Letters. 1989. 433–438. 1

Tang Z., Wu Y., Jia Y., Jiang N. PIV measurements of a turbulent boundary layer perturbed by a wall-mounted transverse circular cylinder element // Flow Turbulence Combust. 2017. 100. 365–390. 1

Testik F.Y., Voropayev S.I., Fernando H.J.S. Flow around a short horizontal bottom cylinder under steady oscillatory flows // Physics of Fluids. 2005. 17, 047103. 1

Thomson J., Polagye B., Durgesh V., Richmond M.C. Measurements of turbulence at two tidal energy sites in Puget Sound, WA // IEEE Journal of oceanic engineering. 2012. 37, 3. 1

Westerweel J., Scarano F. Universal outlier detection for PIV data // Exp. Fluids. 2005. 39. 1096–1100. 2.1

Xu J. Wake interaction of NREL wind turbines using a Lattice Boltzmann Method // Sustainable Energy. 2016. 4. 1–6. 1

Zhong Q., Li D., Chen Q., Wang X. Coherent structures and their interactions in smooth open channel flows // Environmental Fluid Mechanics. 2015. 15. 653–672. 1

Zou Q., He X. On pressure and velocity boundary conditions for the lattice Boltzmann BGK model // Physics of Fluids. 1997. 2.2